A novel biodegradable Zn-0.4Li-0.4Cu alloy with superior strength-ductility synergy and corrosive behavior by laser powder bed fusion

Muhammad Waqas, Dingyong He, Chengxing He, Zhen Tan, Xu Wu, Gang Ji, Xingye Guo

A novel biodegradable Zn-0.4Li-0.4Cu alloy with superior strength-ductility synergy and corrosive behavior by laser powder bed fusion

Muhammad Waqas[1], Dingyong He[1,2], Chengxing He[3,4], Zhen Tan[1], Xu Wu[1], Gang Ji[5], Xingye Guo[1 *]

1 College of Materials Science and Engineering, Beijing University of Technology, 100124, No.100, Ping Le yuan, Beijing, PR China.
2 Beijing Engineering Research Center of Eco-materials and LCA, 100124, No.100, Ping Le yuan, Beijing, PR China;
3. Department of Chemical and Environmental Engineering, School of Engineering and Applied Sciences, Yale University, New Haven, CT 06520, USA;
4. Energy Sciences Institute, Yale University, West Haven, CT 06516, USA
5. Univ. Lille, CNRS, INRAE, Centrale Lille, UMR 8207–UMET–Unité Matériaux et Transformations, Lille, France.

***** Correspondence: xyguo@bjut.edu.cn

Abstract: Zinc (Zn) alloys have recently revolutionized and shown promising usage for degradable biomedical implants (BMI). However, due to the low strength of pure Zn, its application in the biomedical industry was limited. In the current research, an innovative biodegradable Zn-0.4Li-0.4Cu alloy produced by laser powder bed fusion (LPBF) with good mechanical properties was investigated. The Zn-0.4Li-0.4Cu alloy showed superior mechanical properties (tensile strength at 296 MPa, yield strength at260 MPa, and after heat treatment elongation at 8.3%), a record for biodegradable Zn alloys, as a consequence of grain refinement, second-phase precipitation of intermetallic compounds, and solid solution strengthening. The impacts of Cu and Li on the microstructures, mechanical behaviors, corrosive behavior and deterioration rate of the Zn-0.4Li-0.4Cu alloy were studied. The addition of Cu and inherent fast-cooling rate of the LPBF process are favorable for promoting the nucleation events, leading to the refinement of grains. In addition, the formation of the second-phase precipitates ($CuZn_4$ and $ZnLi_4$) in the matrix was founded to further improve the mechanical properties. Moreover, the alloy showed a consistent degradation manner and a suitable degradation rate of 0.023 mm/year. Based on the findings shown above, the biodegradable Zn-0.4Li-0.4Cu alloy can be a potential candidate for vascular stents and medical applications due to its excellent mechanical properties and adequate degrading behavior.

Keywords: Biodegradable Zn-alloy, Mechanical properties, Laser powder bed fusion, Corrosion

1. Introduction

Biodegradable metallic materials, which typically require good mechanical properties, a suitable biodegradation rate, and good biocompatibility, have been given much more attention in recent years[1, 2]. Currently, prevailing biodegradable metals include magnesium (Mg) and its alloys, iron (Fe) and its alloys, and zinc (Zn) and its alloys [3]. Magnesium (Mg) is a popular metallic material, and its alloys have been reported to have strong mechanical and biocompatibility properties, but it has a rapid rate of deterioration [4-6]. Although iron-based alloys have been found to have excellent mechanical properties with a very low rate of degradation, their unfavorable ferromagnetism effect restricts their applications in medical devices [2, 7, 8]. Zinc (Zn) is a biocompatible element and has a typical corrosion potential of -0.8V, which is between iron (-0.4 V) and magnesium (-2.4 V)[9, 10], indicating Zn has an

intermediate degradation rate between the Fe and Mg alloy. As a result, zinc-based alloys have great potential in the application of biodegradable metal implants [11-13]. The corrosion properties of Zn alloys were first investigated by Vojtech et al. [14] where the biodegradable properties of Zn-Mg and Zn-Al-Cu alloys were studied using the simulated body fluids method. According to the findings, the corrosion rates of Zn-Mg and Zn-Al-Cu alloys were 51 mm/year and 221 mm/year, respectively. In a study of the corrosion behavior of as-cast Zn-xMg alloys (x = 1, 2, 3, and 5 wt.%) in NaCl solution [15], it was discovered that the corrosion current density in Zn-3Mg alloy is around 34% higher than that of purified zinc, which was much faster than it required to be.

Pure Zn doesn't meet the standards for medical metal implants, particularly in vascular stents, because as-cast pure zinc has a low tensile strength of around 20 MPa [16]. A beneficial way to improve the mechanical strength of zinc is alloying. In terms of increasing the mechanical properties of zinc-based alloys, it is feasible to combine Zn with recognized biodegradable elemental metals or elements compatible with the human body (e.g., magnesium [17-21], copper [22, 23], calcium [24], strontium [23], iron [25], silver [24], lithium [26], and manganese[27]). For the fabrication of Zn alloy components, various conventional and emerging techniques have been explored, such as hot rolling[28, 29], casting [19, 23], vivo-vitro [25], hot extrusion [22, 30], and laser powder bed fusion (LPBF) [31]. Demir et al. obtained Zn samples with a relative density of 98% by using LPBF and auxiliary Ar purge flows to remove vapors from the Zn samples [32]. A gas circulation mechanism revealed by Wen et al.[33] revealed that this Ar purge process suppressed interference between Zn sample and Zn fume thus stabilizing the LPBF procedure of Zn in a controlled atmosphere.

Lithium (Li) and Copper (Cu) were also demonstrated as an efficient alloying element with Zn to enhance strength. The tensile strength of pure Zn was improved considerably by alloying with Li, while becoming less ductile as the Li percentage increased [34]. Zhao et al. [26] utilized a hot extrusion procedure and produced Zn-xLi alloys with varying Li concentrations (x =0, 0.2, 0.4, and 0.6 wt%) and investigated their mechanical characteristics. The findings demonstrated that when the Li content increased, the microhardness/UTS of hot-rolled Zn-xLi alloy increased from 45 HV/120 MPa to 136 HV/560 MPa, respectively, as the x increased from 0 to 6%. Lan et al.[35] fabricated Zn-2Cu wt.% alloy using the LPBF process, and revealed noticeable enhancements in hardness (84 HV), yield strength (145 MPa), and ultimate tensile strength (188 MPa) through solution strengthening, fine-grain strengthening, and second-phase strengthening. These researches provide a solid theoretical basis for developing biodegradable Zn-based alloys with controlled microstructural features and improved mechanical properties using LPBF. Tong et al. [36] used the hot rolling technique to produce Zn-2Cu-xLi (x=0, 0.4, and 0.8 wt.%) ternary alloys. Within these alloys, Zn-2Cu-0.4Li achieved the best mechanical properties with a TYS of 281 MPa, and UTS of 395 MPa, and demonstrated effective antibacterial properties, making it a promising candidate for bone-implant applications.

Beyond alloying with Lithium and Copper, Liu et al. [37] used LPBF to fabricate bulk Zn-0.8Li-0.1Mg and porous scaffolds with varying porosities to explore their mechanical properties, corrosion behavior, and biocompatibility. The Zn-0.8Li-0.1Mg alloy exhibited significantly higher tensile strength and compressive strength compared to pure Zn, with the P70 scaffolds

showing the best overall performance in osteogenic ability and biocompatibility [37]. With advancements in the LPBF process for pure zinc, optimized LPBF pure-Zn samples nowadays could exhibit a high relative density of 99.86%, UTS of 129MPa, and a high ductility of 1221%, these superior properties are attributed to multiple deformation mechanisms and continuous strain hardening [38].

Given the superior performance demonstrated by Zn-Li and Zn-Cu alloys, coupled with the advancements and flexibility of LPBF technology, it is reasonable to infer that a Zn-Li-Cu alloy produced through LPBF holds the promise as a suitable material for degradable biomedical implants [10, 31, 33]. In this study, Zn-Li-Cu bulk samples were prepared with LPBF technology using an argon-atomized Zn-Li-Cu powder for the first time. The LPBF parameters, microstructures, mechanical properties, and degradation behavior of LPBF-built Zn-Li-Cu alloy were studied. The outcomes of the current work laid the groundwork for further development of LPBF-built Zn-Li-Cu alloys and provided data to help better understand the microstructures, mechanical characteristics, and biodegradation properties of Zn-Li-Cu alloy.

2. Experimental methods

2.1 Specimen preparation

In this study, an argon-atomized Zn-0.4Li-0.4Cu powder was used. Its chemical composition measured by inductively coupled plasma (ICP) was 99.2 wt.% Zn, 0.4 wt.% Li, and 0.4 wt.% Cu. The physical properties of Zn-0.4Li-0.4Cu powder were listed in Table 1. The flow mobility of the powders detected using the Hall flowmeter was 28 seconds per 50 g powders, and the bulk density was 3.15 g/cm^3. The specimen was fabricated with an EOS M100 LPBF 3D-printer (EOS, Germany), equipped with a Yb-fiber laser having a spot diameter of 40 μm. The laser power (LP), scanning speed (SS), and hatch distance (HD) were the primary LPBF parameters optimized in this work to improve the relative density of specimen, as listed in Table 2. The layer thickness of powder was maintained constant at 20 μm. The experiment parameters were optimized using response surface methodology (RSM). The specimen dimensions for metallographic, and tensile analyses were 6×6×6 mm, and 50×5×3 mm, respectively. After LPBF, for comparison test, few of the samples were subjected to annealing process under vacuum in a PKE12/12 furnace (LAC s.r.o., Czech Republic) at 240 °C for one hour, and then cooled to the room temperature within the furnace.

Table 1. Physical properties of Zn-Li-Cu powders.

Mean size of particle (D_{50})	Flow mobility	Bulk density	O_2 (content)
28 μm	28 sec/50g	3.15 g/cm^3	0.019 %

2.2 Microstructure characterization

The specimens for metallographic analysis were polished and etched with 1ml HNO_3 + 50 ml of deionized water. The relative density was measured by Archimedes method and further

analyzed using microstructure image-based method. For the Archimedes method, the porosity and the relative density of the specimens were calculated by the following equation,

$$\rho_r = 100 - \frac{(B-A)D_w}{(B-F)D_o} \times 100 \quad \textbf{(1)}$$

where ρ_r was relative density by volume (%), A was the mass of as-built sample in air (g), B was the mass of sample in oil (g), F was the mass of sample in the water (g), D_o was the density of oil (0.838 g/cm^3, Alfa Aesar H31661 Nujol), D_w was the density of water (0.998 g/cm^3).

To analyze the microstructure using image-based method, eight images were captured for each sample using an optical microscope (OM, Olympus GX51, Japan) to calculate the relative density via the ImageJ software. The phase composition was analyzed using X-ray diffraction (XRD, D8 Advance Bruker, Germany) with Cu k_α radiation, and conducted with an angle range of 30°-90° at a scanning rate of 10^{-2} °/s. A scanning electron microscope (SEM, Quanta-200) equipped with an energy dispersive spectroscopy (EDS) detector was employed to study local phase morphology, chemistry, and distribution. The samples for electron backscatter diffraction (EBSD) measurements were prepared using a Leica EM RES102 ion polishing machine, where the angle of the ion gun was fixed at 4.5°, the working voltage was between 2 kV and 5 kV, the current was 0.8 A, and the polishing time was about 50 minutes. The EBSD tests were performed on a Quanta 650 field emission SEM. The acceleration voltage was set to 30 kV and the step size was in the range of 200-800 nm. The raw experimental data was treated using HKL Channel 5 software.

2.3 Measurement of mechanical properties

A Vickers hardness tester (HXD-1000) was utilized to assess the hardness of the specimens under a load of 100 N with a holding time of 15 seconds. Each specimen (with a dimension of 6×6×6 mm) was assessed at a minimum of five random locations. The samples for the tensile test were designed according to ASTM E8E88-16 standard and built being perpendicular to the building direction, and the dimensions were given in Figure 1. An electronic universal tensile material testing machine (Instron 5985) was used with a strain rate of 3×10^{-3}/sec. Three tests of each sample state were conducted to minimize experimental error.

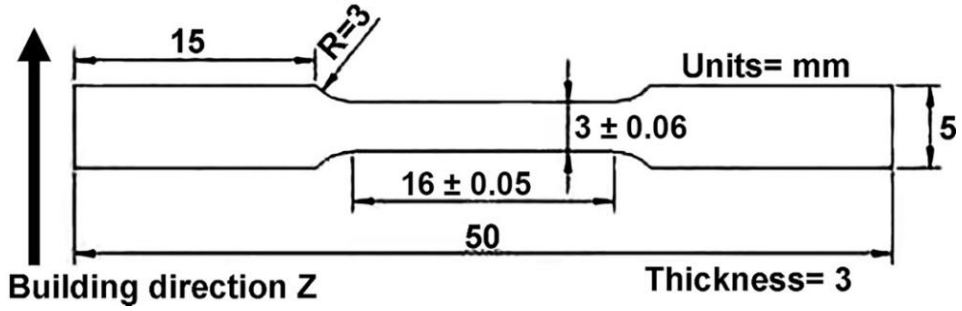

Fig. 1. The shape and dimensions with primary tolerances of the specimen used in the tensile tests.

2.4 Electrochemical and immersion test

Electrochemical tests of LPBF-built Zn-0.4Li-0.4Cu specimens were executed using an electrochemical workstation (Princeton P4000A, AMETEC, USA). The testing samples were cut into a rectangular shape (5×5×10 mm). After the cutting process, the samples were mounted using epoxy so that only one surface was exposed to the electrolyte, and the out-surface was carefully polished with P1000 and P2000 sandpapers. The experiment was carried out with a three-electrode system consisting of a working electrode (Zn-0.4Li-0.4Cu specimen), a reference electrode (silver), and a counter electrode (platinum). In the experiment, both the working and the reference electrodes were parallel to the counter electrode. The open circuit potential was measured when the specimen was immersed in Hank solution (HBSS) for 90 minutes. A potentiodynamic polarization (PDP) test was conducted with a scanning rate of 1 mV/s. By using linear fitting and Tafel interpolation, the corrosion potential (E_{corr}), and corrosion current density (I_{corr}) were computed. Three experiments were conducted for each sample (Zn, Zn-0.4Li-0.4Cu and heat-treated Zn-0.4Li-0.4Cu) to reduce experimental error.

The immersion experiment was conducted according to ASTM-G31-72 guidelines. The Zn-0.4Li-0.4Cu specimens were immersed in Hank's solution using an electric thermostatic water bath equipment at 37°C, pH 7.3 for 21 days. The specimen was cut down into a rectangular shape with a dimension of 10×5×3 mm. An electronic pH meter (Oakton PH 550 Benchtop) was used to record pH values. After the immersion experiment, chromic acid (H_2CrO_4) was utilized to eradicate the corrosion products from the surfaces of the specimens. The weight loss was assessed with an electronic balance with a measuring accuracy of 0.1 mg. Three specimens were evaluated separately for each material (Zn and Zn-0.4Li-0.4Cu) to minimize experimental error.

3. Results and discussion

3.1 Microstructure of the initial powder

As shown in Figure 2, the morphology of the atomized powder particles was quasi-spherical. Locally, a few spherical satellite particles with a size lower than 10 μm were visible, which was typical for gas atomization. The particle size distribution of the powder used for LPBF, measured by a laser particle analyzer, was in the range of 15-54 μm. The average size was around 28 μm.

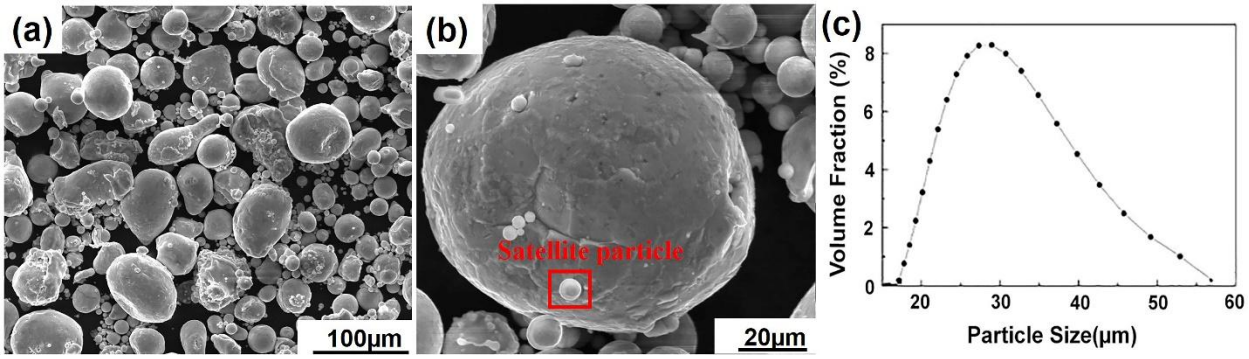

Fig. 2. Morphologies of the Zn-Li-Cu atomized powder characterized by SEM: (a) low-magnification image; (b) high-magnification image highlighting a single particle; (c) Particle size distribution.

3.2 LPBF parameter optimization for full densification

The range of LPBF parameters explored in this paper for the formation of Zn-0.4Li-0.4Cu alloy were laser power from 50 to 60 W, scanning speed from 500 to 700 mm/s, and hatch distance at 0.07 mm. Table 2 gave the relative density (ρ_r) and porosity of the different LPBF-built Zn-0.4Li-0.4Cu samples, as well as the volumetric laser energy density (E_v) for different LPBF parameters. E_v was related to the evaporation volume of the powders, and was calculated with the following equation,

$$E_V = \frac{P}{V*h*d} (J/mm^3) \quad \textbf{(2)}$$

where P was laser power, V indicated scanning speed, h was hatching distance and d was the thickness of the powder bed. In this work, the laser power and scanning speed were chosen as primary variables to optimize the relative density of the Zn-0.4Li-0.4Cu sample and control of the evaporation process, while hatch distance and layer thickness were kept constant at 0.07 mm and 20 μm, respectively.

Table 2. The relative density of different specimens fabricated using different process parameters.

Sr No.	LP (W)	SS (mm/s)	HD (mm)	Density (%)	Porosity (%)	E_v (J/mm^3)
1	47	600	0.07	95.75	4.25	55.95
2	50	500	0.07	96.53	3.47	71.43
3	50	700	0.07	97.31	2.69	51.02
4	55	458	0.07	97.17	2.83	85.78
5	55	600	0.07	97.31	2.69	65.48
6	55	741	0.07	98.64	1.36	53.02
7	60	500	0.07	97.93	2.07	85.71
8	60	600	0.07	98.45	1.55	73.81
9	60	700	0.07	99.45	0.55	61.22

As shown in Figure 3, the cross-sectional microstructure of the as-built specimens with different LPBF parameters was demonstrated. With the increase in E_v, the density of the LPBF-built alloys initially increased before subsequently decreasing. For example, with E_v at 51.02 J/mm^3, the density of the sample was low at 97.31% with many large and irregular pores visible (Figure 3d). With the increase in E_v up to 61.22 J/mm^3, the density of sample No. 9 increased up to the highest value of 99.45%. No visible pores were revealed (Figure 3a). With further increase in E_v up to 85.78 J/mm^3, the porosity of the alloy increased and the density decreased down to 97.17%. These pores were irregularly scattered in terms of size and location (Figure 3h). The primary reason for the existence of the pores in these Zn-0.4Li-0.4Cu at high E_v samples was the

massive evaporation that occurred due to the high laser energy input. Sample No. 9 was the densest one, which was heat treated and subjected to detailed microstructure characterization and properties tests as presented hereafter.

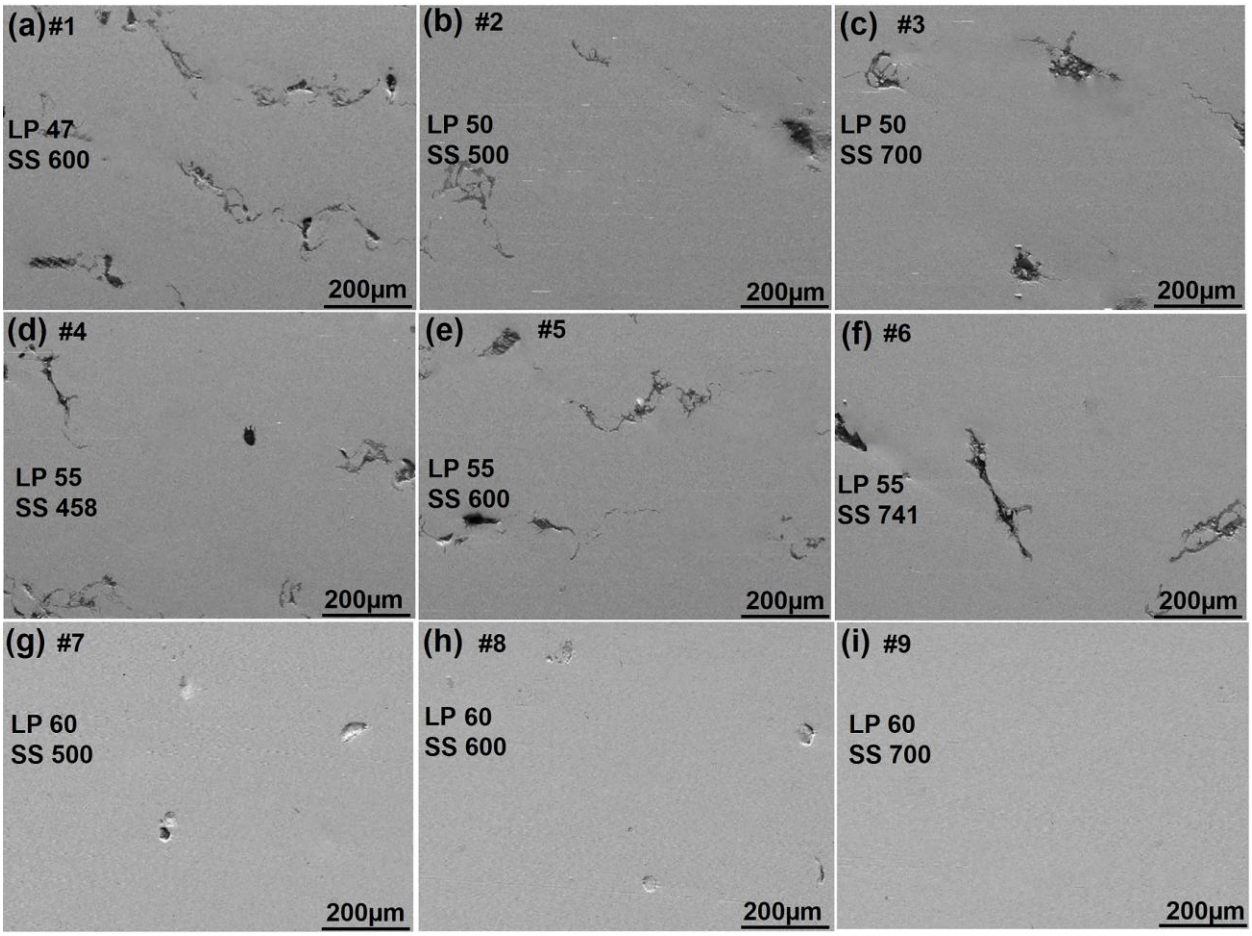

Fig. 3. The morphologies of LPBF built Zn-Li-Cu alloy parts fabricated with different volumetric laser energy density (E_v) contributed by different laser power (LP), scanning speeds (SS), and fixed hatch distance (HD) 0.07 mm.

3.3 Microstructure of the LPBF-processed and heat-treated samples

The XRD results of the Zn-0.4Li-0.4Cu feedstock powders, as-built and heat-treated samples are shown in Figure 4. It is well known that pure Zn and its alloys contain a hexagonal closed-pack structure and can be distinguished in the XRD pattern [19]. As indicated in Figure 4, $CuZn_4$ and $LiZn_4$ phases were present in the as-built and heat-treated samples but were very limited in the feedstock powder, suggesting that many intermetallic compounds were generated during the LPBF process. As an important hardening phase in the Zn-Li-Cu system, it was reported that the $LiZn_4$ could improve the strength but greatly reduce the ductility of the LPBF-built specimen [20]. The contents of $CuZn_4$ and $ZnLi_4$ phases in the as-built samples were higher than those in

the heat-treated samples, indicating the heat-treatment process reduced the intermetallic compounds.

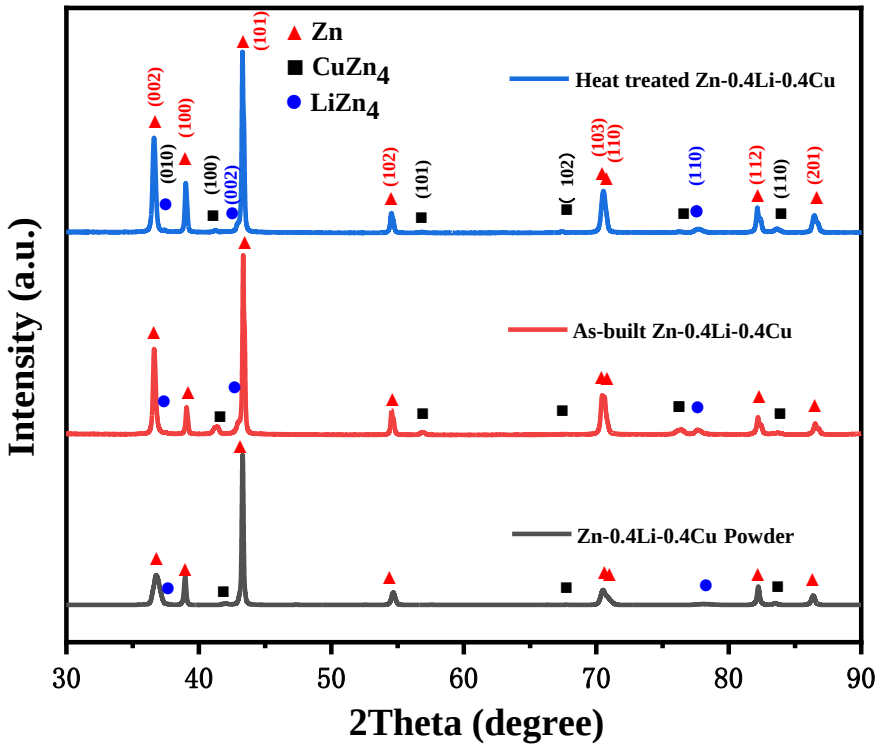

Fig. 4. XRD patterns of the Zn-0.4Li-0.4Cu feedstock powder, as-built and heat-treated samples.

The SEM and EBSD were used to characterize the microstructure of pure Zn (for comparison) and Zn-0.4Li-0.4Cu samples, as shown in Figures 5, 6, and 7. The Zn-0.4Li-0.4Cu alloy was mainly composed of α-Zn matrix with the intermetallic compounds dispersed along the grain boundaries. After analyzing the Zn-Li-Cu phase diagram and EBSD tests, it was confirmed that the intermetallic compounds $LiZn_4$ and $CuZn_4$ were dispersed in the matrix of Zn. Many nano-size particles were observed in Figure 6 (g and h). These dispersed nanoparticles could contribute to increasing the ductility in the alloy by mitigating stress concentration. Furthermore, nanoprecipitates are crucial in enhancing the strength of various alloys, as previously reported [39, 40]. In the alloy under investigation, the $CuZn_4$ precipitates and the matrix Zn exhibited a coherent interface and similar crystal structures, facilitating dislocation slip across the grains [41]. Similarly, to the $LiZn_4$ phase, the $CuZn_4$ is characterized by disorder and classified as an electron compound (mostly metallic bonding), as a result, its plastic deformability is comparable to that of the Zn matrix. The $LiZn_4$ and $CuZn_4$ intermetallic phases are disordered phases with a hexagonal closed-pack structure (P63/mmc) [42]. As displayed with EDS mapping in Figure 6 (d, e, and f), Zn and Cu were uniformly distributed in the alloy. As shown in Figure 6 (a and g), $CuZn_4$ and $LiZn_4$ phases precipitated as needle-shaped formations, which were highlighted in yellow and green color in Fig 6 (h). Although Li is a light element and was not detectable by

EDS, Figure 4 and Figure 6 (g) confirmed the presence of $LiZn_4$ phase in Zn-0.4Li-0.4Cu alloy, aligning with findings from prior studies in Zn-Li and Zn-Cu-Li alloys [26, 40]. The precipitation of $LiZn_4$ around the primary Zn matrix could be attributed to the eutectoid reaction [43, 44]. The analysis of grain size in Zn-0.4Li-0.4Cu alloy was given in Figure 6 (c). Inverse pole figure (IPF) with low magnification, and phase graphs with high magnification are given in Figure 6 (b) and (g) respectively. Kernel average misorientation (KAM) map and geometrically necessary dislocation (GND) density graph were provided in figure 6 (i and j).

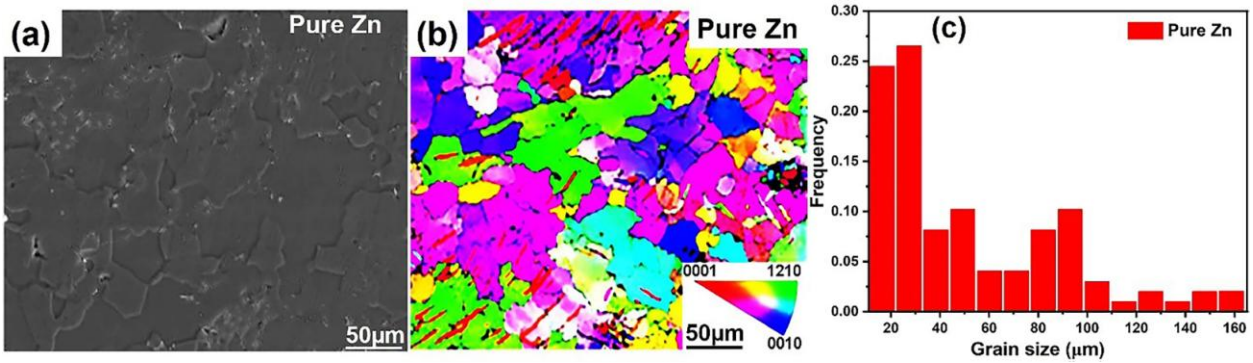

Fig. 5. Microstructures of as-built pure Zn analyzed with EBSD, SEM and EDS: (a) SEM image of pure Zn, (b) IPF map of pure Zn (c) grain size of pure Zn.

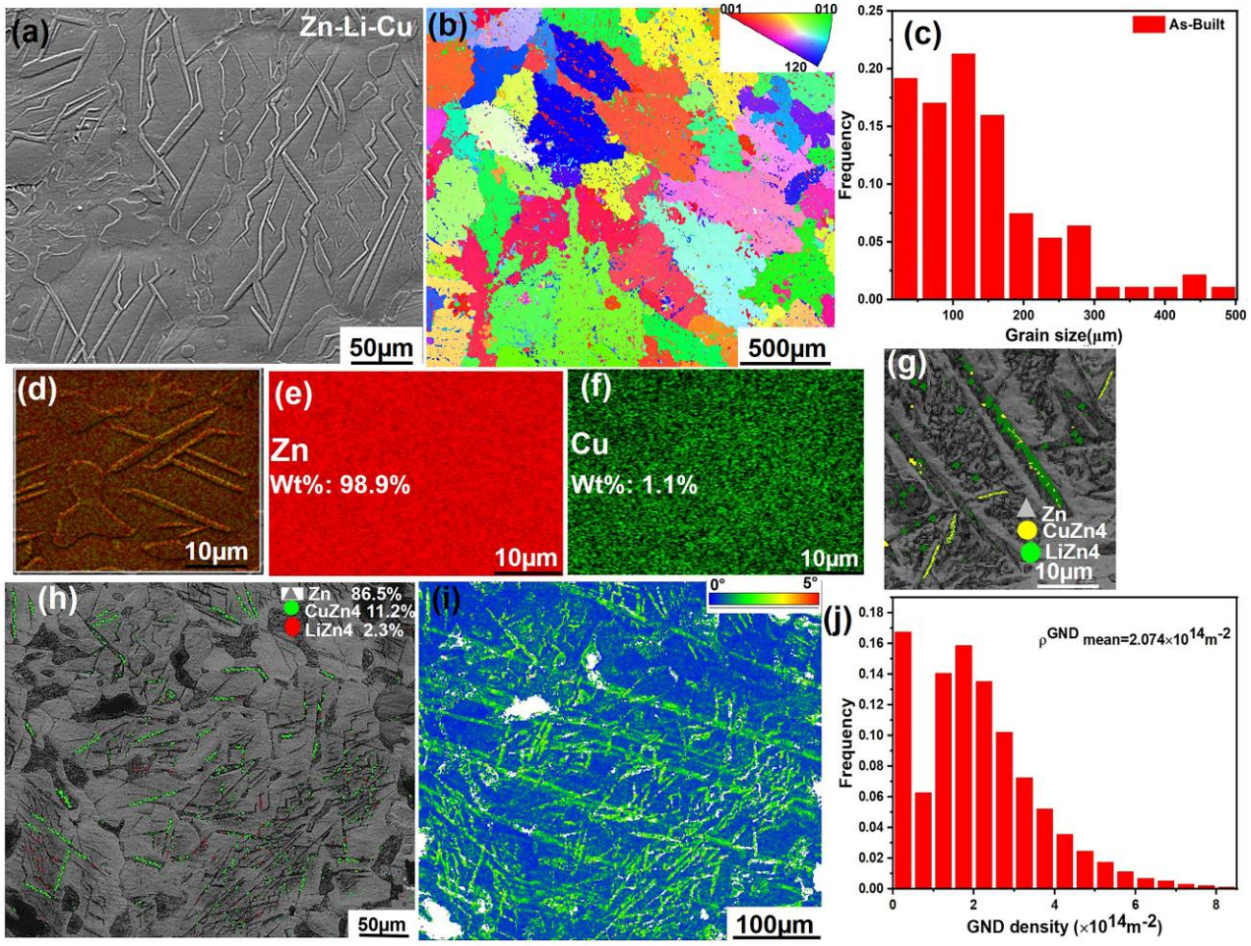

Fig. 6. Microstructure analysis of the as-built Zn-0.4Li-0.4Cu alloy analyzed with SEM, EDS and EBSD: (a) high magnification SEM images showing the grain boundaries as well as precipitation of α-$ZnCu_4$ and α-$LiZn_4$, (b) IPF map of Zn-0.4Li-0.4Cu, (c) grain size statistics of Zn-0.4Li-0.4Cu, (d, e, and f) EDS elemental mapping of elements Zn and Cu, (g and h) EBSD phase map, and (I and j) KAM map and GND density distribution.

The grain size graph was depicted in Figure 7 (c). The size of the grains in Figure 7 was larger than that of Figure 6 (c), indicating a slight growth of the grains during the heat treatment. Figures (d), (e), and (f) in Figures 6 and 7 displayed the elemental mapping of Zn and Cu elements. As shown in Figure 6, many needle-like intermetallic compounds were formed. Comparing the heat-treated specimen in Figure 7 with the as-LPBF-built specimen in Figure 6, there were the less needle-like intermetallic compounds existed, and more island-like intermetallic compounds generated in the heat-treated specimen, which indicated the great difference in morphology between the as-LPBF-built and the heat-treated specimens. Moreover, the concentration of precipitation phases ($ZnLi_4$ and $CuZn_4$) was reduced after the heat treatment due to the diffusion and solution of Li and Cu elements in the solid solution phase of Zn.

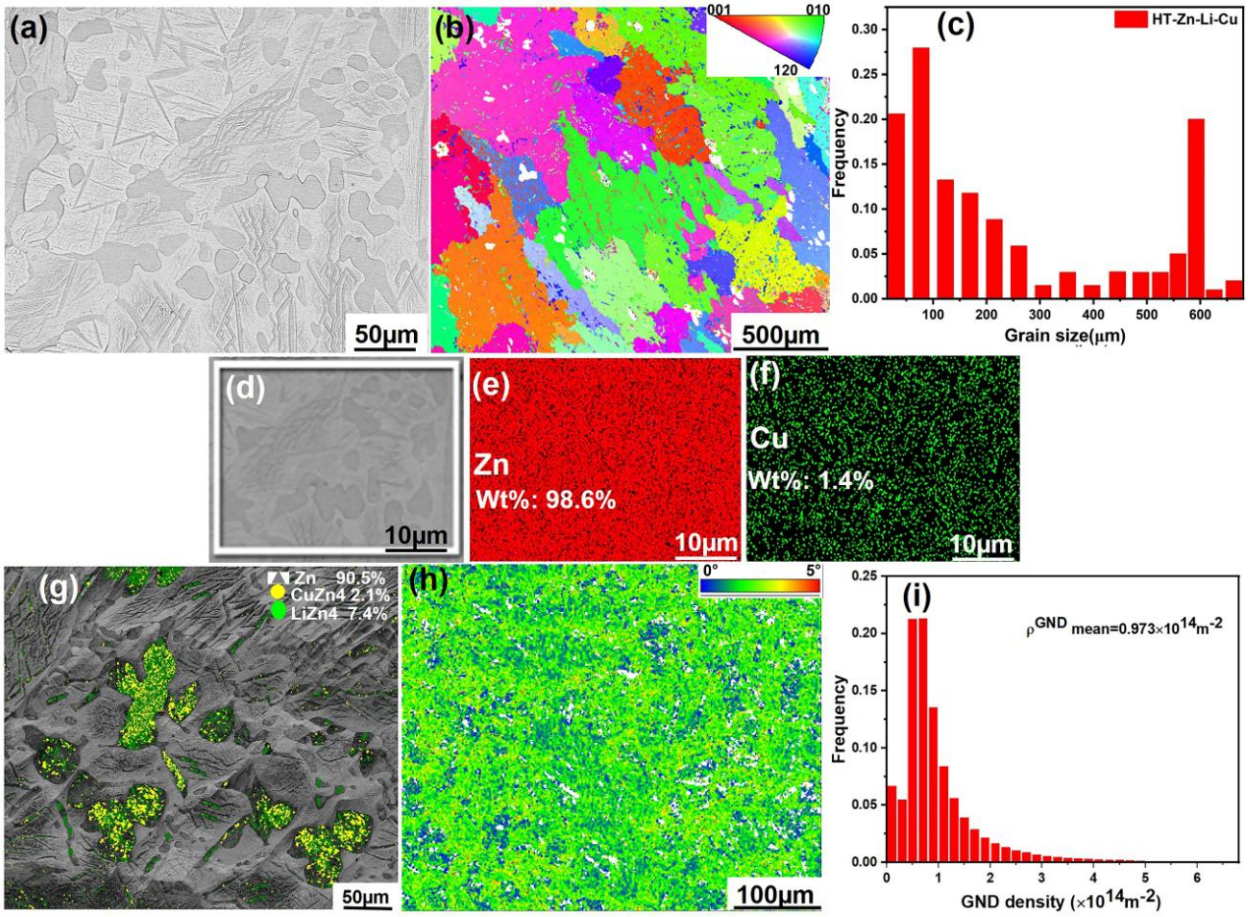

Fig. 7. Microstructure analysis of Zn-0.4Li-0.4Cu alloy after the heat treatment: (a) high magnification SEM images showing the grain boundaries as well as precipitation of α-$ZnCu_4$ and α-$LiZn_4$, (b) IPF map with low resolution, (c) grain size statistics, (d) SEM image with the area that EDS scanned,

(e and f) EDS elemental mapping of elements Zn and Cu, (g) EBSD phase map, and (h and i) KAM map and GND density distribution.

KAM map and GND density graph before and after the heat treatment were provided in Figure 6(h and i) and Figure 7 (h and i). The GND density was calculated as following equation,

$$\rho_{GND} = \frac{2\theta}{\mu b} \quad (3)$$

where ρ_{GND} represented the GND density, θ represented local crystal misorientation, μ step size length during scanning EBSD (6000 nm), and b was the magnitude of the Burgers vector 0.271 nm[42]. According to the dislocation strengthening theory, high-density dislocation led to dislocation entanglement, hindered the dislocation movement, and improved the deformation resistance of alloys [42]. The reduced dislocation density in heat-treated samples was one of the reasons leading to the increased ductility of Zn-0.4Li-0.4Cu samples.

The precipitation of the LPBF-prepared Zn-0.4Li-0.4Cu alloy was examined using a transmission electron microscope (TEM). Bright-field (BF) TEM images of Zn-0.4Li-0.4Cu alloys before and after heat treatment were shown in Figure 8 (a and c), while the selected area electron diffraction (SAED) patterns of the precipitates were presented in Figure 8 (b and d). These intermetallic compounds were identified as $LiZn_4$ and $CuZn_4$. Both phases ($LiZn_4$ and $CuZn_4$) were characterized by a hexagonal close-packed structure but with different lattice parameters (a = 0.267 nm, c = 4.765 nm for $LiZn_4$), and (a = 0.266 nm, c = 4.53 nm for $CuZn_4$), respectively. During the elemental analysis, Li was not detected but the presence of $LiZn_4$ phase confirmed the existence of element Li in the alloy. The presence of $LiZn_4$ and $CuZn_4$ phases confirmed through TEM analysis, was consistent with the results shown in Figures 4, 6, and 7. The concentration of the $LiZn_4$ (2.2%) phase was lower than that of the $CuZn_4$ (8.4%) phase. It is worth noting that the measured Cu content in the precipitates and matrix is slightly higher than the actual amount due to potential contamination from Cu signals originating from the Cu sample stage during the TEM testing. The presence of both $LiZn_4$ and $CuZn_4$ phases was also reported in recent investigations on Zn-Li-Cu alloys [43]. The dislocation characterization before and after the heat treatment was presented in Figure 8(e and f). A high density of dislocations, primarily near the grain boundaries (GB), was observed in Figure 8e. These dislocations interacted and tangled, forming distinct dislocation cells near the GB with low internal density, indicated by yellow arrows. With heat treatment, further dislocation piled up and tangles subdivided the original grain into smaller parts, making individual dislocations indistinguishable. As the number of dislocations at the cell borders increased, they interacted and rearranged to form low-angle grain boundaries (LAGBs) through recovery. The ~100nm grains in Figure 8e were subdivided into fine grains by LAGBs in Figure 8f, consistent with EBSD results. Figure 8f demonstrated the newly formed fine grains were uniformly distributed, indicating the reduction of dislocation. Note a few dislocations remain within these new grains due to further deformation.

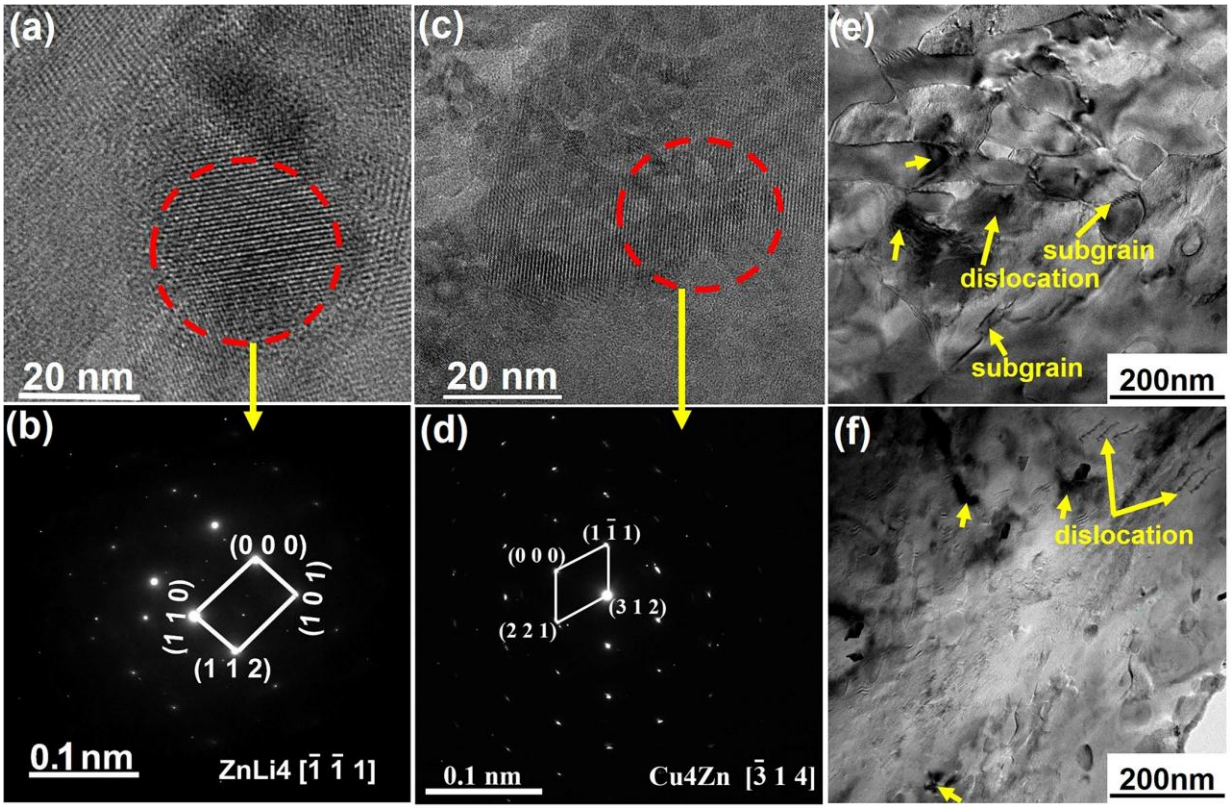

Fig. 8. Transmission electron microscope (TEM) characterization and selected area electron diffraction (SAED) analysis of Zn-0.4Li-0.4Cu wt.% alloy before and after heat treatment: (a and c) TEM images, (b and d) patterns of SAED, (e and f) bright-field TEM image.

3.4 Mechanical properties of the LPBF-processed and heat-treated samples

As shown in Figure 9, the hardness values of the pure Zn, as-built Zn-0.4Li-0.4Cu, and heat-treated Zn-0.4Li-0.4Cu samples were 53 $HV_{0.1}$, and 151 $HV_{0.1}$, and 101 $HV_{0.1}$ respectively. A slight addition of Cu and Li to the Zn-0.4Li-0.4Cu alloy made the Zn alloy two to three times harder compared to that of pure Zn. The existence of $CuZn_4$ and $ZnLi_4$ in the Zn matrix promoted the strengthening effect and effectively improved the hardness of the alloy, according to results reported by other researchers [39, 41, 45]. The heat treatment process made the material ductile due to the diffusion of Li and Cu into the base material, thus decreasing the hardness and strength of the alloy. The dislocation density was measured to be quite substantial with the GND density value of $2.074\pm0.21\times10^{14}$ m^{-2}, due to high-temperature gradients during the LPBF process. The elevated thermal gradients during LPBF processing led to increased strain localization, which is managed through a higher dislocation density, as reported previously [44, 46, 47].

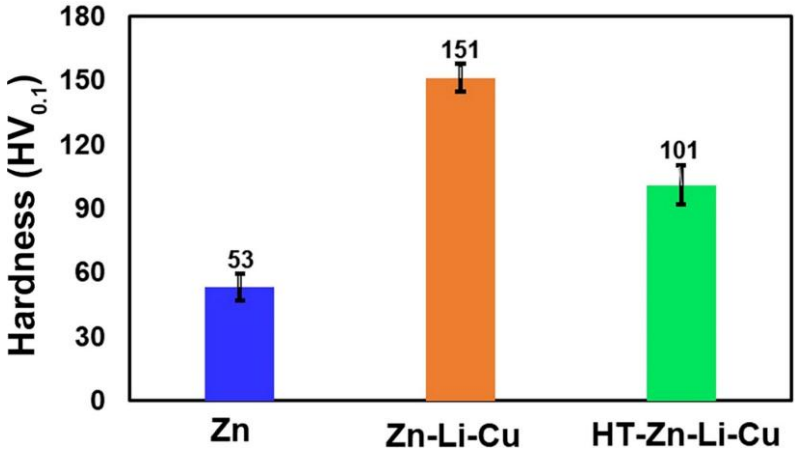

Fig. 9. Microhardness comparison between pure Zn, and LPBF built Zn-0.4Li-0.4Cu alloy before and after heat treatment.

For the ultimate tensile strength (UTS) test, the samples were fabricated with the optimal parameters (laser power 60 W, scan speed 700 mm/s, hatch distance 0.07 mm). Three parallel tests were conducted for samples fabricated under the same condition on the universal tensile test machine, and the mean value was selected for the tensile stress-strain curve. The tensile properties of as-built and heat-treated LPBF Zn-0.4Li-0.4Cu samples, as well as LPBF pure Zn samples, were listed in Table 3. The mechanical properties of these materials were displayed in Figure 10(a). The UTS strength of as-built Zn-0.4Li-0.4Cu alloy reached 296 MPa, which was almost three times the UTS strength of pure Zn at 110 MPa. The heat-treated sample had a UTS strength of 201 MPa, lower than the as-built sample, but the elongation increased from 3.6% to 8.3%, due to the reduction of the residual stress and dislocation density, the recovery of the microstructure [48]. As a consequence, the ductility of the alloy increased while its strength decreased, as expected from the strength-ductility trade-off [48, 49]. The addition of Li and Cu introduced different metallic phases ($CuZn_4$ and $LiZn_4$) to the alloy, resulting in basic hardening effects.

Table 3. Mechanical properties of LPBF-built and post-treated pure Zn and Zn-Li-Cu samples.

Methods and Specimens	UTS (MPa)	0.2%off set (MPa)	YM (GPa)	El (%)
As-built Zn-Li-Cu	296±1	260	56.32	3.6±0.1
Post-treated Zn-Li-Cu	201±1	156	53.02	8.3±0.2
As-built pure Zn	110±2	80	37.56	9.2±0. 03

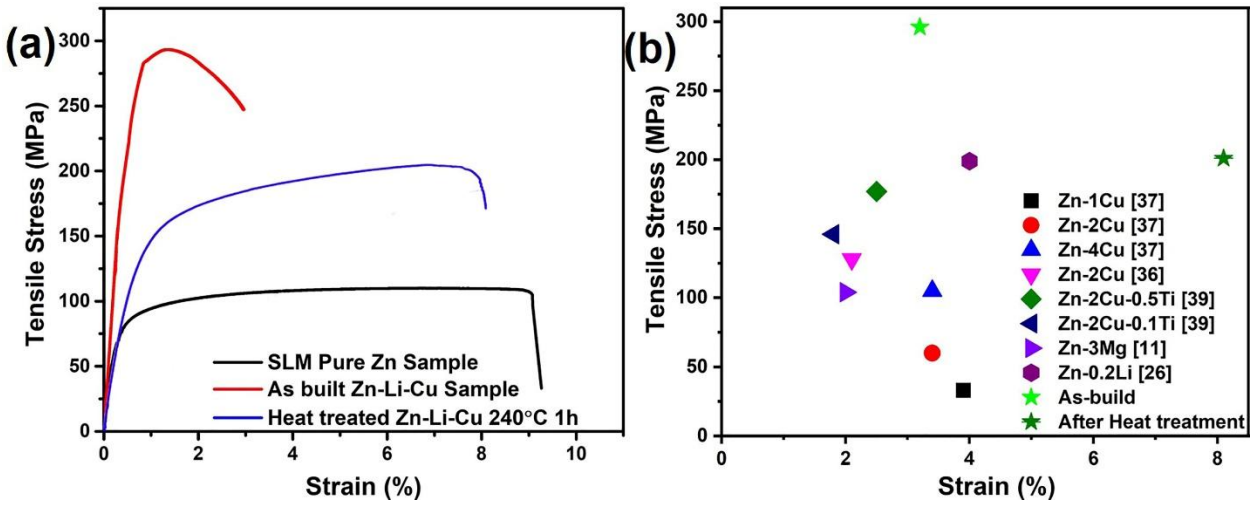

Fig. 10. Comparison of the tensile strength and ductility of alloys studied in this work with previously reported biodegradable Zn alloys.

As shown in Figure 10 (b), the comparison of tensile strength and ductility of different Zn-based alloys was illustrated. The Zn-0.4Li-0.4Cu alloy demonstrated superior strength and reasonable ductility compared with previously reported additive-manufactured zinc alloys [39, 50]. The ternary Cu and Li-based zinc alloys demonstrated in this paper could achieve greater strength in comparison with Zn-Li [19, 25], Zn-Cu [39, 43, 45], and Zn-Mg-based alloys [15, 23].

As shown in Figure 11, the fracture morphologies of pure Zn and Zn-Li-Cu samples were demonstrated. Based on the SEM images, pores, cracks, steps, tear ridges, river patterns, secondary cracks, and unmelted powders could be observed on the surfaces of both pure Zn and Zn-0.4Li-0.4Cu samples, suggesting natural cleavage. In the pure Zn and as-built Zn-0.4Li-0.4Cu samples, no dimples were observed, indicating a brittle deformation, in compliance with the low ductility measured with these samples. The development of pores in the LPBF specimens was because the gases could not escape in time, or Li as a light element, might evaporated at high temperatures. Besides, these tiny pores could act as initialization points of fractures, or lead to the generation of cracks during the tensile experiments. As shown in Figure 11 (e and f), the fracture surface of heat-treated Zn-0.4Li-0.4Cu alloy samples captured by SEM was depicted. These images had noticeably fewer, and smaller pores and cracks compared to as-built pure Zn and as-built Zn-0.4Li-0.4Cu alloy samples, which was attributed to the diffusion and solution of metal elements, as well as the reorganization of the internal structure during the low-temperature heat treatment process. Figure 11 (e and f) also showed some dimples, indicating improved ductility.

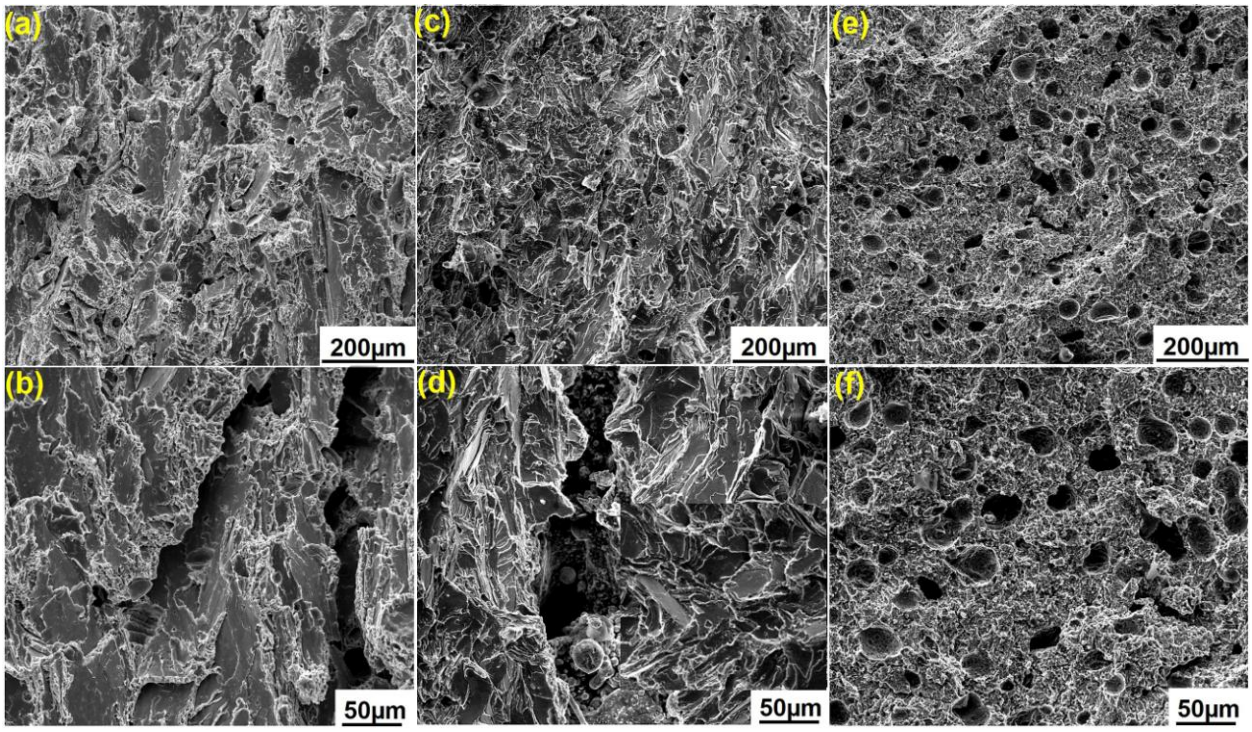

Fig. 11. SEM images depicting the fracture surfaces of (a-b) pure Zn, (c-d) as-built Zn-0.4Li-0.4Cu and (e-f) heat-treated Zn-0.4Li-0.4Cu samples.

3.5 Strengthening mechanism

For the Zn-0.4Li-0.4Cu alloy, the yield strength can be calculated considering the grain boundary strengthening ($\Delta\sigma_{gb}$), solid solution ($\Delta\sigma_{ss}$), shear strength strengthening (σ_{ppt}), and dislocation density contribution ($\Delta\sigma_{Dis}$). The σ_{ys} is described by the following equation [42, 47].

$$\sigma_{ys} = \Delta\sigma_{gb} + \Delta\sigma_{ss} + \sigma_{sp} + \Delta\sigma_{Dis} \quad \textbf{(4)}$$

The Hall-Petch [42] relationship describes the increase in yield strength due to grain boundary strengthening with the following equation.

$$\Delta\sigma_{gb} = \sigma_0 + k_y d^{-1/2} \quad \textbf{(5)}$$

Here friction stress (σ_0) for Zn is reported to be 20 MPa [51], k_y is the Hall-Petch coefficient at 220 MPa.μm$^{1/2}$ and d is the average grain size of $CuZn_4$ in as-built Zn-Li-Cu sample is 76μm, which is calculated from Figure 6(h) by length. These values contribute to the $\Delta\sigma_{gb}$ is 45.24 MPa. The solid solution strengthening contributed by lattice distortions induced by the addition of Li and Cu can be calculated by the following equation [42],

$$\Delta\sigma_{ss} = (k_{Li}^{\frac{3}{2}} c_{Li} + k_{Cu}^{\frac{3}{2}} c_{Cu})^{2/3} \quad \textbf{(6)}$$

where k_{Li} (661.2 MPa) and k_{Cu} (483.7 MPa) [29] are the strengthening constants, c represents the solute contents which is 0.4% for Li and 0.4% for Cu. Summarizing these values, the attained result of $\Delta\sigma_{ss}$ is 106.92 MPa. The strength contribution from the second-phase precipitations

(σ_{sp}) like $LiZn_4$ and $CuZn_4$ to the Zn-Li-Cu alloy was investigated by Zhang et al. [42], which is 104.30 MPa. The increase in yield strength is also contributed by the increase of the dislocation density due to plastic deformation. $\Delta\sigma_{Dis}$ is described as the following equation [52],

$$\Delta\sigma_{Dis} = \alpha * G * b * \sqrt{\rho} \quad \textbf{(8)}$$

where α is a constant of 0.3, G is the shear modulus of Zn-Li-Cu at 36.1 GPa [42], b is Burger's vector calculated to be 2.71×10^{-10} m, and ρ is dislocation density at $2.07\times10^{14}m^{-2}$, which was calculated from the GND results, as shown in Figure 6j. These values contribute to a $\Delta\sigma_{Dis}$ of 42.22 MPa. By summing the contributions to the yield strength from different mechanisms, the calculated σ_{ys} is 298.68 MPa (45.24+106.92+104.30+42.22) which is relatively close to the experimental value of 260MPa for the as-built Zn-0.4Li-0.4Cu alloy with about 14.8% errors.

3.6 Electrochemical and immersion results

Electrochemical experiments were performed to analyze the biodegrading resistance behaviors of LPBF-built Zn-0.4Li-0.4Cu alloy in Hank solution with pH 7.4, as shown in Figure 12. The potentiodynamic polarizing (PDP) curves of Zn-0.4Li-0.4Cu samples before and after heat treatment were plotted, as shown in Figure 12 (a). The Tafel extrapolation approach was applied to calculate the corrosion potential E_{corr} and current density I_{corr}, as listed in Table 4. The corrosion potential of the as-built Zn-0.4Li-0.4Cu alloy was higher than the pure Zn sample[53]. In contrast, the heat-treated sample showed decreased corrosion potential, due to the reorganization of the internal structure and weak bonding of the intermetallic phases. During the corrosion process, passivation behavior was observed, as evidenced by the current plateau in their anodic polarization. This phenomenon was also found for pure Zn in earlier reported work. Generally, Zn-0.4Li-0.4Cu alloys exhibited high I_{corr} or higher corrosion rates compared to reported Zn biodegradable alloys [39, 41, 45], this high electrochemical activity was attributed to the large number of lattice flaws after deformation. The comparison of electrochemical properties between Zn-xCu, Zn-2Cu, and Zn-0.4Li-0.4Cu alloys was presented in Table 4, where Zn-0.4Li-0.4Cu exhibited less negative E_{corr} than Zn-xCu and Zn-2Cu alloys [40, 43]. Additionally, the electrochemical impedance spectroscopy (EIS) response of the specimens showed that the semicircle radius of the Zn-0.4Li-0.4Cu alloy was higher than that of pure Zn, suggesting an improvement in corrosion resistance.

Table 4. Electrochemical properties of LPBF Zn-0.4Li-0.4Cu alloys compared to other Zn-based biodegradable alloys in literature results

Electrochemical properties	As built Zn-0.4Li-0.4Cu	Heat treated Zn-0.4Li-0.4Cu	Pure Zn	Zn-xCu [43]	Zn-2Cu[40]
OCP (VRef)	-1.012 ± 0.011	-1.079 ± 0.021	-1.6071±0.015	-1.067 ± 0.013	-1.091±0.009
E_{Corr} (VRef)	-1.098 ± 0.002	-1.175 ± 0.054	-1.453±0.016	-1.352 ± 0.005	-1.255±0.031
I_{corr} (μA/cm^2)	11.356 ± 3.214	13.275 ± 3.892	11.152±2.461	13.546± 4.965	15.012±11.03

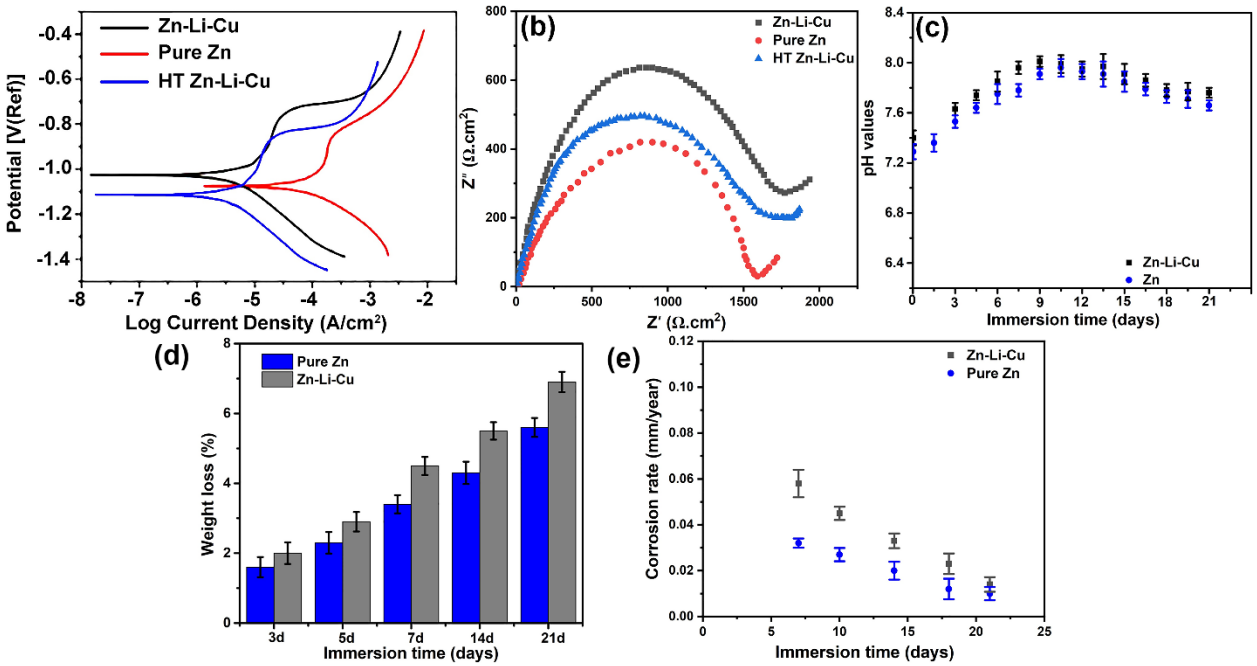

Fig. 12. Electrochemical and corrosion characterization of pure Zn and Zn-0.4Li-0.4Cu specimens: (a) PDP curve; (b) Nyquist plot; (c) pH values during immersion test; (d) weight loss of specimens during immersion test; (e) corrosion rates.

The change in pH values in the Hank solution during the immersion test was documented in Figure 12 (c). The pH variation was observed during the first eight days of the immersion test for all the specimens. After several days, the pH value gradually stabilized. The weight loss during the immersion tests up to 21 days for pure Zn and Zn-0.4Li-0.4Cu alloy samples was displayed in Figure 12 (d). As shown in Figure 12 (e), the quantitative corrosion rate analysis based on the weight loss was plotted. These figures illustrated that the corrosion rates of pure Zn and Zn-0.4Li-0.4Cu alloy decreased with the increasing immersion time. The corrosion rates decreased rapidly during the initial days, and decreased only slightly in the later stage of the immersion test. Similarly, the error bars for the corrosion rates of pure Zn and Zn-0.4Li-0.4Cu alloy were big at the initial stage of the immersion test, and became smaller at the latter stages. This indicated that corrosion was significantly influenced by the condition of the sample surface and the stability of the oxide films. The Zn-0.4Li-0.4Cu alloy showed a faster corrosion rate compared to the pure Zn sample, and this was consistent with the electrochemical characterization of the specimens (Figure 11 (c)), suggesting the electrochemical reaction dominated the corrosion. Shi et al. [43] investigated the corrosion behavior of Zn-Cu alloys and reported a corrosion rate of 0.055±0.005 mm/year after 14 days of immersion. The corrosion rate of Zn-0.4Li-0.4Cu was 0.023±0.003 mm/year in this work after the 21-day immersion. The corrosion rate of zinc alloys in this work showed a similar trend as reported in the previous research, where the corrosion rate slowly decreases with the increase of immersion time.

4. Conclusions

In this study, a novel biodegradable Zn-0.4Li-0.4Cu alloy with superior mechanical properties was prepared using LPBF technology. The key findings are presented as follows:

1. The highest density of the LPBF fabricated Zn-0.4Li-0.4Cu alloy reached 99.45%, and the optimal parameters for reaching this were laser power at 60 W, scanning speed at 700 mm/s, and hatch distance at 0.07 mm.

2. The LPBF-built Zn-0.4Li-0.4Cu alloy demonstrated superior mechanical strength, reasonable ductility, and satisfactory degradation rate. This alloy could be a potential candidate for fabricating biodegradable metal implants. In this work, the as-LPBF-built specimen showed an ultimate tensile strength of 296 MPa, a tensile yield strength of 260 MPa, and a total elongation of 3.2%. After the heat treatment process, the UTS of the alloy was reduced to 201 MPa but the elongation was increased to 8.1%. The degradation rate of Zn-0.4Li-0.4Cu alloy after immersing in Hank solution for 21 days was 0.023 mm/year.

3. The superior mechanical properties of the as-LPBF-built Zn-0.4Li-0.4Cu alloy can be attributed to the precipitation of the intermetallic compounds $CuZn_4$ and $ZnLi_4$. The increase in elongation can be attributed to the change of the intermetallic compound morphology from the needle-shape-dominated precipitation to the island-shape-dominated precipitation.

Acknowledge: The authors would like to thank the financial support for this work from the General Program of Science and Technology Development Project of Beijing Municipal Education Commission (KM202010005006).

References

[1] X. Zhuo, Y. Wu, J. Ju, H. Liu, J. Jiang, Z. Hu, J. Bai, F. Xue, Recent progress of novel biodegradable zinc alloys: From the perspective of strengthening and toughening, Journal of Materials Research and Technology, (2022).
[2] C. Ji, A. Ma, J. Jiang, D. Song, H. Liu, S. Guo, Research status and future prospects of biodegradable Zn-Mg alloys, Journal of Alloys and Compounds, (2024) 174669.
[3] M. Luqman, Y. Ali, M.M.Y. Zaghloul, F.A. Sheikh, V. Chan, A. Abdal-hay, Grain refinement mechanism and its effect on mechanical properties and biodegradation behaviors of Zn alloys–A review, Journal of Materials Research and Technology, (2023).
[4] Z.-Y. Zhang, H. Tian, L. Bian, S.-Z. Liu, Y. Liu, Z.-L. Wang, Cu-Zn-based alloy/oxide interfaces for enhanced electroreduction of CO2 to C2+ products, Journal of Energy Chemistry, 83 (2023) 90-97.
[5] X. Tong, Y. Han, R. Zhou, W. Jiang, L. Zhu, Y. Li, S. Huang, J. Ma, C. Wen, J. Lin, Biodegradable Zn–Dy binary alloys with high strength, ductility, cytocompatibility, and antibacterial ability for bone-implant applications, Acta Biomaterialia, 155 (2023) 684-702.
[6] R. Li, Y. Ding, H. Zhang, X. Wang, Y. Gao, J. Xu, Toward high strength and large strain hardening Zn alloys via a novel multiscale-heterostructure strategy, Materials Science and Engineering: A, 899 (2024) 146410.

[7] H. Liu, L. Ye, K. Ren, C. Sun, X. Zhuo, K. Yan, J. Ju, J. Jiang, F. Xue, J. Bai, Evolutions of CuZn5 and Mg2Zn11 phases during ECAP and their impact on mechanical properties of Zn–Cu–Mg alloys, Journal of Materials Research and Technology, 21 (2022) 5032-5044.
[8] Y. Zhao, H. Li, Y. Liu, Y. Huang, Precipitation Behavior, Recrystallization Behavior, and Mechanical Properties of Highly Alloyed Al-Zn-Mg-Cu Alloy with Respect to Zn/Mg Ratio, Journal of Materials Engineering and Performance, (2023) 1-16.
[9] R. Huang, H. Yang, P. Sun, S. Zheng, M. Li, Y. Duan, Effects of Mg contents on microstructures and corrosion behaviors of homogenization Al-Zn-Mg-Cu alloys, Corrosion Science, 223 (2023) 111461.
[10] Y. Chen, P. Wen, M. Voshage, L. Jauer, Y. Qin, J.H. Schleifenbaum, R. Poprawe, Laser additive manufacturing of Zn metal parts for biodegradable implants: Effect of gas flow on evaporation and formation quality, Journal of Laser Applications, 31 (2019) 022304.
[11] W. Yuan, D. Xia, S. Wu, Y. Zheng, Z. Guan, J.V. Rau, A review on current research status of the surface modification of Zn-based biodegradable metals, Bioactive materials, 7 (2022) 192-216.
[12] H. Li, Y. Huang, X. Ji, C. Wen, L.-N. Wang, Fatigue and corrosion fatigue behaviors of biodegradable Zn-Li and Zn-Cu-Li under physiological conditions, Journal of Materials Science & Technology, 131 (2022) 48-59.
[13] H. Li, J. Huang, P. Zhang, Q. Zhang, Investigation on tribological behaviors of biodegradable pure Zn and Zn-X (Li, Cu, Ge) binary alloys, Journal of Materials Science: Materials in Medicine, 32 (2021) 149.
[14] D. Vojtěch, J. Kubásek, J. Šerák, P. Novák, Mechanical and corrosion properties of newly developed biodegradable Zn-based alloys for bone fixation, Acta biomaterialia, 7 (2011) 3515-3522.
[15] C. Yao, Z. Wang, S.L. Tay, T. Zhu, W. Gao, Effects of Mg on microstructure and corrosion properties of Zn–Mg alloy, Journal of Alloys and Compounds, 602 (2014) 101-107.
[16] Y. Qin, P. Wen, H. Guo, D. Xia, Y. Zheng, L. Jauer, R. Poprawe, M. Voshage, J.H. Schleifenbaum, Additive manufacturing of biodegradable metals: Current research status and future perspectives, Acta biomaterialia, 98 (2019) 3-22.
[17] E. Mostaed, M. Sikora-Jasinska, A. Mostaed, S. Loffredo, A. Demir, B. Previtali, D. Mantovani, R. Beanland, M. Vedani, Novel Zn-based alloys for biodegradable stent applications: Design, development and in vitro degradation, Journal of the mechanical behavior of biomedical materials, 60 (2016) 581-602.
[18] A.J. Drelich, S. Zhao, R.J. Guillory II, J.W. Drelich, J. Goldman, Long-term surveillance of zinc implant in murine artery: Surprisingly steady biocorrosion rate, Acta biomaterialia, 58 (2017) 539-549.
[19] G. Katarivas Levy, J. Goldman, E. Aghion, The prospects of zinc as a structural material for biodegradable implants—a review paper, Metals, 7 (2017) 402.
[20] E. Mostaed, M. Sikora-Jasinska, J.W. Drelich, M. Vedani, Zinc-based alloys for degradable vascular stent applications, Acta biomaterialia, 71 (2018) 1-23.
[21] Y. Li, Y. Wang, B. Lu, W. Yu, H. Wang, G. Xu, Z. Wang, Effect of Cu content and Zn/Mg ratio on microstructure and mechanical properties of Al–Zn–Mg–Cu alloys, Journal of Materials Research and Technology, 19 (2022) 3451-3460.
[22] C. Shuai, Z. Dong, C. He, W. Yang, S. Peng, Y. Yang, F. Qi, A peritectic phase refines the microstructure and enhances Zn implants, Journal of Materials Research and Technology, 9 (2020) 2623-2634.
[23] H. Li, X. Xie, Y.F. Zheng, Y. Cong, F. Zhou, K. Qiu, X. Wang, S. Chen, L. Huang, L. Tian, Development of biodegradable Zn-1X binary alloys with nutrient alloying elements Mg, Ca and Sr, Scientific reports, 5 (2015) 10719.
[24] C. Shuai, L. Xue, C. Gao, Y. Yang, S. Peng, Y. Zhang, Selective laser melting of Zn–Ag alloys for bone repair: microstructure, mechanical properties and degradation behaviour, Virtual and Physical Prototyping, 13 (2018) 146-154.
[25] H. Yang, B. Jia, Z. Zhang, X. Qu, G. Li, W. Lin, D. Zhu, K. Dai, Y. Zheng, Alloying design of biodegradable zinc as promising bone implants for load-bearing applications, Nature communications, 11 (2020) 401.

[26] S. Zhao, C.T. McNamara, P.K. Bowen, N. Verhun, J.P. Braykovich, J. Goldman, J.W. Drelich, Structural characteristics and in vitro biodegradation of a novel Zn-Li alloy prepared by induction melting and hot rolling, Metallurgical and Materials Transactions A, 48 (2017) 1204-1215.
[27] M. Yang, S. Liu, Y. Zhang, J. Tang, M. Zhang, Mechanism for enhanced precipitation strengthening due to the addition of copper to Al-Zn-Mg alloys with high Zn/Mg ratio, Materials & Design, 234 (2023) 112295.
[28] Y. Zou, X. Wu, S. Tang, Q. Zhu, H. Song, M. Guo, L. Cao, Investigation on microstructure and mechanical properties of Al-Zn-Mg-Cu alloys with various Zn/Mg ratios, Journal of Materials Science & Technology, 85 (2021) 106-117.
[29] C. Chen, S. Fan, J. Niu, H. Huang, Z. Jin, L. Kong, D. Zhu, G. Yuan, Alloying design strategy for biodegradable zinc alloys based on first-principles study of solid solution strengthening, Materials & Design, 204 (2021) 109676.
[30] J. Kubásek, D. Vojtěch, E. Jablonská, I. Pospíšilová, J. Lipov, T. Ruml, Structure, mechanical characteristics and in vitro degradation, cytotoxicity, genotoxicity and mutagenicity of novel biodegradable Zn–Mg alloys, Materials Science and Engineering: C, 58 (2016) 24-35.
[31] Y. Yang, F. Yuan, C. Gao, P. Feng, L. Xue, S. He, C. Shuai, A combined strategy to enhance the properties of Zn by laser rapid solidification and laser alloying, Journal of the mechanical behavior of biomedical materials, 82 (2018) 51-60.
[32] A.G. Demir, L. Monguzzi, B. Previtali, Selective laser melting of pure Zn with high density for biodegradable implant manufacturing, Additive Manufacturing, 15 (2017) 20-28.
[33] P. Wen, L. Jauer, M. Voshage, Y. Chen, R. Poprawe, J.H. Schleifenbaum, Densification behavior of pure Zn metal parts produced by selective laser melting for manufacturing biodegradable implants, Journal of Materials Processing Technology, 258 (2018) 128-137.
[34] G.-N. Li, S.-M. Zhu, J.-F. Nie, Y. Zheng, Z. Sun, Investigating the stress corrosion cracking of a biodegradable Zn-0.8 wt% Li alloy in simulated body fluid, Bioactive materials, 6 (2021) 1468-1478.
[35] C. Lan, Y. Hu, C. Wang, W. Li, X. Gao, X. Lin, Phase formation and strengthening mechanism of Zn–2 wt% Cu alloy fabricated by laser powder bed fusion, Additive Manufacturing, 85 (2024) 104153.
[36] X. Tong, T. Shen, X. Zhou, J. Zeng, J. Tao, K. Munir, Y. Li, S. Huang, X. Wu, J. Ma, Biodegradable Zn–Cu–Li alloys with ultrahigh strength, ductility, antibacterial ability, cytocompatibility, and suitable degradation rate for potential bone-implant applications, Smart Materials in Manufacturing, 1 (2023) 100012.
[37] A. Liu, Y. Lu, J. Dai, P. Wen, D. Xia, Y. Zheng, Mechanical properties, in vitro biodegradable behavior, biocompatibility and osteogenic ability of additively manufactured Zn-0.8 Li-0.1 Mg alloy scaffolds, Biomaterials Advances, 153 (2023) 213571.
[38] Z. Dong, C. Han, Y. Zhao, J. Huang, C. Ling, G. Hu, Y. Wang, D. Wang, C. Song, Y. Yang, Role of heterogenous microstructure and deformation behavior in achieving superior strength-ductility synergy in zinc fabricated via laser powder bed fusion, International Journal of Extreme Manufacturing, 6 (2024) 045003.
[39] L. Li, C. Liu, H. Jiao, L. Yang, F. Cao, X. Wang, J. Cui, Investigation on microstructures, mechanical properties and in vitro corrosion behavior of novel biodegradable Zn-2Cu-0.01 Ti-xLi alloys, Journal of Alloys and Compounds, 888 (2021) 161529.
[40] Z. Li, Z.-Z. Shi, Y. Hao, H.-F. Li, H.-J. Zhang, X.-F. Liu, L.-N. Wang, Insight into role and mechanism of Li on the key aspects of biodegradable ZnLi alloys: Microstructure evolution, mechanical properties, corrosion behavior and cytotoxicity, Materials Science and Engineering: C, 114 (2020) 111049.
[41] J. Lin, X. Tong, K. Wang, Z. Shi, Y. Li, M. Dargusch, C. Wen, Biodegradable Zn–3Cu and Zn–3Cu–0.2 Ti alloys with ultrahigh ductility and antibacterial ability for orthopedic applications, Journal of Materials Science & Technology, 68 (2021) 76-90.
[42] X. Zhang, G. Liu, L. Jiang, D. Jiao, J. Jiang, C. Chen, Z. Gao, J. Niu, G. Sha, Y. Shen, Hierarchical structured Zn-Cu-Li alloy with high strength and ductility and its deformation mechanisms, International Journal of Plasticity, 169 (2023) 103731.

[43] S. Huang, L. Wang, Y. Zheng, L. Qiao, Y. Yan, In vitro degradation behavior of novel Zn–Cu–Li alloys: Roles of alloy composition and rolling processing, Materials & Design, 212 (2021) 110288.
[44] K. Prasad, M. Obana, A. Ito, S. Torizuka, Synchrotron diffraction characterization of dislocation density in additively manufactured IN 718 superalloy, Materials Characterization, 179 (2021) 111379.
[45] P. Li, W. Zhang, J. Dai, A.B. Xepapadeas, E. Schweizer, D. Alexander, L. Scheideler, C. Zhou, H. Zhang, G. Wan, Investigation of zinc‐ copper alloys as potential materials for craniomaxillofacial osteosynthesis implants, Materials Science and Engineering: C, 103 (2019) 109826.
[46] K. Bertsch, G.M. De Bellefon, B. Kuehl, D. Thoma, Origin of dislocation structures in an additively manufactured austenitic stainless steel 316L, Acta Materialia, 199 (2020) 19-33.
[47] K. Prasad, Y. Horita, A. Ito, S. Torizuka, In situ synchrotron diffraction study of a crack-free additively manufactured Ni base superalloy, Scripta Materialia, 200 (2021) 113896.
[48] Y. Mine, S. Matsumoto, Z. Horita, Strengthening and hydrogen embrittlement of ultrafine-grained Fe–0.01 mass% C alloy processed by high-pressure torsion, Corrosion science, 53 (2011) 2969-2977.
[49] B. He, B. Hu, H. Yen, G. Cheng, Z. Wang, H. Luo, M. Huang, High dislocation density–induced large ductility in deformed and partitioned steels, Science, 357 (2017) 1029-1032.
[50] L. Zhang, X. Liu, H. Huang, W. Zhan, Effects of Ti on microstructure, mechanical properties and biodegradation behavior of Zn-Cu alloy, Materials Letters, 244 (2019) 119-122.
[51] Z.C. Cordero, B.E. Knight, C.A. Schuh, Six decades of the Hall–Petch effect–a survey of grain-size strengthening studies on pure metals, International Materials Reviews, 61 (2016) 495-512.
[52] N. Krasilnikov, W. Lojkowski, Z. Pakiela, R. Valiev, Tensile strength and ductility of ultra-fine-grained nickel processed by severe plastic deformation, Materials Science and Engineering: A, 397 (2005) 330-337.
[53] H. Jiang, H. Xing, Z. Xu, B. Yang, E. Liang, J. Zhang, B. Sun, Effect of Zn content and Sc, Zr addition on microstructure and mechanical properties of Al-Zn-Mg-Cu alloys, Journal of Alloys and Compounds, 947 (2023) 169246.